**Title page**

# Spatiotemporal histological changes observed in mouse subcutaneous tissues during the foreign body reaction to silicone

Sao Oe[1,#], Md. Abdul Masum[1,2,#], Osamu Ichii[1,3,*], Takanori Nishimura[3,4], Teppei Nakamura[1,5], Takashi Namba[1], Yuki Otani[1], Yasuhide Nakayama[6], Yaser Hosny Ali Elewa[1,7], and Yasuhiro Kon[1]

1. Laboratory of Anatomy, Department of Basic Veterinary Sciences, Faculty of Veterinary Medicine, Hokkaido University, Sapporo, Japan
2. Department of Anatomy, Histology and Physiology, Faculty of Animal Science and Veterinary Medicine, Sher-e-Bangla Agricultural University, Dhaka, Bangladesh
3. Laboratory of Agrobiomedical Science, Faculty of Agriculture, Hokkaido University, Sapporo, Japan
4. Laboratory of Cell and Tissue Biology, Research Faculty of Agriculture, Hokkaido University, Sapporo, Japan
5. Section of Biological Safety Research, Chitose Laboratory, Japan Food Research Laboratories, Chitose, Japan
6. Biotube Co. Ltd, Tokyo, Japan
7. Department of Histology, Faculty of Veterinary Medicine, Zagazig University, Zagazig, Egypt

[#]Equal contribution

[*]Corresponding author:
Osamu Ichii, D.V.M, Ph.D.
Laboratory of Anatomy, Department of Basic Veterinary Sciences, Faculty of Veterinary Medicine, Hokkaido University, Kita 18, Nishi 9, Kita-ku, Sapporo 060-0818, Japan
Email: ichi-o@vetmed.hokudai.ac.jp
Tel: +81-11-706-5189; Fax: +81-11-706-5189

**Abstract**

We investigated spatiotemporal changes in host tissues during foreign body reactions. Silicone tube was subcutaneously embedded into ICR mice, and tissue surrounding silicone (TSS) was observed at 2, 7, 14, 21, 28, 43, and 70 days (D) post-surgery. The thin layer (TL) and loose connective tissues (LCTs) (inside and outside the TSS) developed until D21 and densified afterward. Neutrophils infiltrated the TSS until D14 and formed neutrophil extracellular traps (NETs) in the TL during D7-21. In the LCTs, mast cell counts increased until D21, and macrophage numbers peaked at D14. Several macrophages showed LYVE-1 expression, supporting a tissue-remodeling role. Developmental indices of collagen fibers (CFs) and reticular fibers (RFs) increased during D2-21. NETs, but not neutrophils, were detected after D28. Mast cell numbers peaked at D43 and were maintained until D70. Myofibroblasts consistently localized to the TL from D14. During D21-28, the area of connective tissue (CNT), and CFs and RFs decreased and increased, respectively, and both remained constant during D28-70. The CF density remained constant from D21 and increased at D70. Thus, TSS showed two phases: inflammation and CNT development (D2-21), and inflammation convergence and CNT stabilization (D28-70). These results provide insights into foreign body reactions in clinical cases.

**Short title**: Foreign body reaction to silicone in mice

**Keywords**: foreign body reaction, silicone, inflammation, fibrosis, neutrophil extracellular traps

## Introduction

In human and animal clinical cases, tissue reactions to embedded materials are crucial, as observed in the case of sutures remaining after being used to surgically close incised wounds. These host reactions are known as foreign body/matter reactions. In particular, problems related to the inflammatory response to foreign bodies are serious in the field of orthopedics. The biocompatibility of biomaterials, such as artificial joints or bone cements, to injured or diseased bones has been carefully evaluated in patients and experimental animals [(1)]. The texture of implant materials affects the formation and histological structure of capsule forms surrounding the implant due to foreign body reactions [(2)]. Histological alterations induced by foreign body reactions may impair the accurate functioning of embedded biosensors, such as subcutaneous glucose sensors or pacemakers. Indeed, several researchers have previously reported that intravenously implanted glucose biosensors do not accurately reflect the glucose level due to foreign body reactions [(3)]. Briefly, it was reported that the sensor sensitivity declined, and a difference was observed between the measured values and the actual values in the blood. Furthermore, in veterinary clinical medicine, microchips are commonly embedded in dogs and cats for identification. However, the development of liposarcoma at the site of an implanted microchip has been reported in previous clinical cases [(4)].

The quality of embedded materials also affects their biocompatibility. In general, silk [(5)] and nylon [(6)] are used for sutures, and metals [(7)], such as titanium [(8)], are used in artificial joints or prosthetic implants. Among the biomaterials, silicone is widely used in the medical field because of its high biocompatibility [(9)]; this includes its use in pacemakers [(10)], arteriovenous shunts in dialysis, or in plastic surgery. Silicone has also been used for long-term indwelling devices implanted during subcutaneous ureteral bypass for the surgical treatment of ureterolithiasis in felines [(11)]. However, these biomaterials also cause foreign body reactions that degrade or encapsulate biomaterials. The degradation of foreign bodies involves angiogenesis with chemotactic factors and inflammation, which includes cell infiltrations of neutrophils, macrophages, and lymphocytes [(12)]. The role of macrophages via phagocytosis is crucial during this process. Recently, it has been suggested that the formation of neutrophil extracellular traps (NETs) also plays an important role in innate immune reactions to foreign bodies, particularly pathogens [(13)]. Furthermore, in cases where the foreign body is not degraded owing to its large size or the presence of less reactive materials, such as silicones, fibrosis-based encapsulation is observed. Briefly, fibroblasts and myofibroblasts migrate, proliferate, and produce the extracellular matrix containing collagens [(14),(15)]. This results in the

formation of a capsule consisting of a collagen-rich extracellular matrix that covers the foreign body and serves to isolate it from the surrounding tissue [9]. The crucial cell populations and the molecules associated with the progression of foreign body reactions have been gradually elucidated, but their spatiotemporal changes, especially the transition from inflammation to fibrosis, have not yet been fully clarified.

In addition to the harmful side of foreign body reactions, they also have beneficial effects in the medical field. Recently, a technique employing foreign body reaction-based encapsulation to produce autologous or allogenic implantable tissues has been reported; this technique is known as in-body tissue architecture technology (iBTA) [9],[16]. Briefly, this is achieved by embedding rod-shaped molds—mainly composed of silicone—into subcutaneous pouches. Connective tissues then develop to cover the molds after a few months. After collection of the molds with the surrounding tissues, the separated tube-like connective tissues—mainly composed of collagens—can be shaped and applied to various transplantations. iBTA produces various kinds of connective tissues applicable for transplantation into blood vessels [17]–[19], as well as the heart valve, cornea, diaphragm, and esophagus. Histologically, some aspects of foreign body reactions against silicone-based molds are still unknown, particularly the timing required to complete the formation of dense and developed fibrous tissue (stable fibrosis). It is important to evaluate the completion of implantable tissues, to enable earlier delivery of the artificial graft and reduce the burden of host-embedded molds.

Foreign body reactions can thus function as a double-edged sword, with harmful and beneficial aspects in both human and veterinary medicine. Therefore, a study focusing on the processes involved in foreign body reactions, including inflammation and fibrosis, is needed to elucidate its pathogenesis and advance the medical technology based on iBTA. This study investigated the spatiotemporal dynamics of the histological changes occurring in tissues surrounding a silicone tube embedded subcutaneously into mice.

## Materials and Methods

### Animals

Male Slc:ICR mice were purchased from Japan SLC, Inc. (Hamamatsu, Japan) and maintained under specific pathogen-free conditions. Animal experiments were approved by the Institutional Animal Care and Use Committee of the Graduate School of Veterinary Medicine, Hokkaido University (approval no. 17-0133). The animals were handled in accordance with the Guide for the Care and Use of Laboratory Animals, Graduate School of Veterinary Medicine, Hokkaido University (approved by the Association for Assessment and Accreditation of Laboratory Animal Care International).

### Surgical embedding of the silicone tube

At 8 weeks of age, mice were anesthetized by intraperitoneal injection (i.p.) of a mixture of medetomidine (0.3 mg/kg), midazolam (4 mg/kg), and butorphanol (5 mg/kg). The dorsal skin was then shaved and disinfected, and an approximately 5 mm long incision was made according to the left–right axis of the mouse. A sterilized silicone tube (1 mm × 20 mm) was embedded into the subcutaneous pouch. The incised wound was closed antiseptically using an absorbable suture (M684R, Matsudaika Kogyo Co., Ltd; Tokyo, Japan), and mice were recovered by injection of atipamezole (0.3 mg/kg, i.p.) under warm conditions. After these treatments, ampicillin (1 mg/kg, i.p.) was administered as an antibiotic once immediately after surgery. At 2, 7, 14, 21, 28, 43, or 70 days (D) post-surgery, mice were euthanized by cutting the femoral artery, followed by cervical dislocation under deep anesthesia, and the skin samples with silicone tubes were collected. The silicone tube was easily collected as it was weakly attached to the subcutaneous tissues, as described previously [9].

### Histological analysis

Collected samples were fixed in 4% paraformaldehyde at 4 °C overnight, embedded in paraffin, and cut into sections (3 μm thick), including the cross section of embedded silicone tube in the rostral direction. Deparaffinized sections were stained with hematoxylin–eosin, Masson’s trichrome, toluidine blue, or picrosirius red (ScyTek Laboratories; Logan, UT, USA).

### Immunohistochemistry (IHC) and immunofluorescence (IF)

IHC for Gr-1, MMTV LTR integration site 4 (PAD4), Iba-1, CD3, B220, CD31, lymphatic vessel endothelial hyaluronan receptor 1 (LYVE-1), neuron-specific class III beta-tubulin (Tuj-1), and alpha smooth muscle actin (α-SMA) was performed to detect

granulocytes, NETs [13], macrophages, T cells, B cells, vascular endothelial cells, lymphatic vessels, neurons, and myofibroblasts, respectively, according to a previous study [20]. Paraffin sections were deparaffinized and antigen retrieval performed. Subsequently, to block internal peroxidase activity, sections were soaked in methanol containing 0.3% $H_2O_2$ for 20 min at 25 °C. After washing three times in phosphate-buffered saline (PBS), the sections were incubated with a blocking serum for 1 h at 25 °C to block non-specific reactions. Then, sections were incubated with primary antibodies overnight at 4 °C. The sections were then washed three times in PBS, incubated with secondary antibodies for 30 min at 25 °C, and washed three times in PBS. Consequently, the sections were incubated with streptavidin-conjugated horseradish peroxidase (SABPO kit, Nichirei; Tokyo, Japan) for 30 min at 25 °C, washed three times in PBS, and the immunopositive reaction visualized with 10 mg 3,3′-diaminobenzidine tetrahydrochloride in 50 mL 0.05 M Tris-$H_2O_2$ solution. Finally, the sections were stained with hematoxylin. The details of the antibodies, antigen retrieval, and blocking are listed in Table 1.

IF was performed to detect LYVE-1- or Iba-1-positive cells. The paraffin sections were deparaffinized, subjected to antigen retrieval, and then blocked using normal donkey serum, using the same protocol as that for IHC. After overnight incubation with the primary antibody, sections were incubated with secondary antibody for 1 h at 25 °C. The sections were observed under a fluorescence microscope (BZX-710, Keyence; Osaka, Japan). The details of antigen retrieval, and the source and dilution of antibodies are listed in Table 1.

**Histoplanimetry**

*Thickness of tissue surrounding silicone tube (TSS) and the thin layer (TL)*

Hematoxylin and eosin-stained sections were converted to virtual slides by Nano Zoomer 2.0 RS (Hamamatsu Photonics Co., Ltd.; Hamamatsu, Japan), and then each measurement was performed using NDP.view2 (Hamamatsu Photonics Co., Ltd.). As the TSS was composed of two layers, TL and loose connective tissue (LCT) from the side attached to the silicone tube, the thicknesses of the TSS and TL were measured separately. Briefly, a line vertically crossing the skin through the center of the silicone tube was drawn, and the length from the silicone tube surface to the end of the LCT was measured along this line. This measurement was performed in one section from each sample, and TSS thickness was compared between the skin side and the visceral side along this line. The TL was easily distinguished from the LCT as a dense layer in the TSS, and TL thickness was also measured in a similar manner to that used for TSS.

*Number of immune cells in the TSS*

For mast cells, toluidine blue-stained sections were converted to virtual slides by Nano Zoomer 2.0 RS, and then each measurement was performed using NDP.view2. The number of metachromatic mast cells was counted in the TSS for one section in each sample. For IHC of Iba-1 or LYVE-1, the number of positive cells was counted using BZ-X710 and BZ-H3C (Keyence). This value was divided by the measured area and expressed as the cell density (number/mm$^2$). For LYVE-1 staining, positive cells that did not form vessel structures were counted. These measurements were performed in three randomized areas on one section of the TSS in each sample.

*Indices for collagen and reticular fiber development in the TSS*

For collagenous fibers, Masson's trichrome-stained sections were converted to virtual slides by Nano Zoomer 2.0 RS, and digital images were obtained by NDP.view2. These were then converted into binary images by GIMP2 (https://www.gimp.org/): the aniline blue-positive area was converted to white and the remaining area to black. The total area and integrated density of the white-colored area in the TSS were measured using ImageJ [(21)], reported as the total area and the density of collagen fibers (CFs), respectively. The total area and density of CFs were measured in one entire section or three randomized areas on the same section, respectively, in each sample.

The picrosirius red-stained sections were observed using BZ-X710 under polarized light (Keyence). The red-, green-, or yellow-colored areas were measured as CFs, reticular fibers (RFs), or the fibers containing both, respectively, using BZ-X710 and BZ-H3C in five randomized areas on a single section in each sample.

**Statistical analysis**

Results are expressed as the mean ± standard error (SE) and analyzed by non-parametric statistical methods. The Kruskal–Wallis test was used to compare the numerical results, and multiple comparisons were performed using Dunnett's test (vs. D2) when significant differences were observed ($P < 0.05$).

## Results

### Morphological alterations in the TSS

Figure 1 shows hematoxylin and eosin-stained cross sections of the TSS with skin and summarizes the histological alterations in the TSS following surgery. Normal skin structure was observed in naïve mice (Fig. 1A). On all examined days, the TSS was observed to cover the silicone tube, and the silicone tube was usually detached from the slide glasses during the sectioning or staining process. Under low magnification (Fig. 1A), the TSS was observed as thin and LCT at D2 and D7 and appeared to develop further from D14 (Fig. 1A). In particular, from D28, the TSS increased perpendicular to the viscera–skin axis. From D28 to D70, no marked alterations were observed under low magnification, but the skin tended to bend along the shape of the silicone tube at these time points, indicating a strong connection between the TSS and skin via connective tissues.

Higher magnification also revealed normal cutaneous muscle and its underlying structure in naïve mice (Fig. 1B). Under high magnification (Fig. 1B), the silicone tube was directly covered by the TL, composed of a single layer of cells; the LCT, containing several scattered mononuclear cells and reticular tissues, was observed outside the TL at D2. The LCT at D2 appeared thick due to increased intercellular spaces. From D7 to D21, the TL was composed of spindle- to round-shaped cells, and the LCT increased in cell number and density. The TL and LCT in the TSS appeared thickest at D21 of the observation period, but the cell numbers in the LCT differed among samples, indicating individual differences in inflammatory conditions. Furthermore, the thickness of the TL or LCT and the intercellular fibrous tissues seemed to decrease and increase, respectively, from D28 to D70. The morphology of the TSS was similar throughout the observation period, and the TL, composed of mainly spindle-shaped cells, and the LCT, including scattered mononuclear cells, were observed. Vascular structures and nerve fibers were observed in resident subcutaneous tissues, and in the TSS formed after silicone tube embedding; no remarkable changes in these were observed during the observation periods.

Based on these findings, in the subsequent analysis we divided the observation periods into 2 phases, namely, the reaction phase showing drastic changes in TSS structures with inflammation (D2-21), and the stable phase showing the development of fibrous tissues in the TSS without severe inflammation (D28-70).

### Inflammatory features of the TSS during the reaction phase

We didn’t observe any change in naïve mice during the reaction phase (Figure not shown). But inflammatory cells were examined in the reaction phase, from D2 to D21

(Fig. 2). A few CD3$^+$ T cells and B220$^+$ B cells were detected in the LCT, especially around the blood vessels, but there were no obvious quantitative changes between the examined days (Fig. 2A and B). Gr-1$^+$ granulocytes, with a nuclear morphology suggestive of neutrophils, tended to localize to the LCT from D2 to D14, but were scarce at D21 (Fig. 2C). Furthermore, at D7 and D14, several Gr-1$^+$ neutrophils lined the inside of the TL. For neutrophils, the formation of NETs was also evaluated by PAD4 (Fig. 2D), a key factor for the citrullination of histones required for NET progression. Recently, it was shown that neutrophils can release net-like structures composed of histone-coated DNA, and this process of NET formation is also called NETosis [13]. We found that PAD4$^+$ neutrophils were mainly observed in the TL at D7 and D14, and D21 samples also retained the PAD4$^+$ reactions, indicating the formation of NETs in the TL during the reaction phase. In toluidine blue staining, metachromatic mast cells were observed in the LCT in the reaction phase, and the number of mast cells tended to increase with time after surgery (Fig. 2E). Iba-1$^+$ macrophages, showing spindle or round shapes, were observed mainly in the LCT in the reaction phase, and their number tended to increase with time after surgery (Fig. 2F).

**Structural components of the TSS in the reaction phase**

Angiogenesis and neurogenesis in the TSS were examined by IHC in the reaction phase, from D2 to D21 (Fig. 3A-C). CD31$^+$ vascular endothelial cells and Tuj-1$^+$ neurons were observed in the resident subcutaneous tissues, and these cells were also seen in the TSS formed after silicone embedding, but there were no marked differences between the examined days (Fig. 3A and B). A few LYVE-1$^+$ lymphatic endothelial cells forming a lumen were detected in the remaining subcutaneous tissues. Furthermore, LYVE-1$^+$ mononuclear cells that did not form vessel structures were scattered in the LCT (Fig. 3C). Compared to D2, the number of LYVE-1$^+$ mononuclear cells appeared higher at D7-21. In addition, α-SMA$^+$ myofibroblasts transformed from activated fibroblasts [22] were examined and detected in the TL from D14 during the reaction phase; they showed a fusiform shape and lined the inside of the TL (Fig. 3D). The development of fibrous tissues in the TSS was examined by Masson's trichrome and picrosirius red staining (Fig. 3E and F). In both stainings, the skin developed a stronger positive reaction than the subcutis. In the picrosirius red staining, the skin showed strong red birefringence, while the subcutis showed a combination of red, yellow, and green birefringence (Fig. 3F). Aniline blue$^+$ CFs from Masson's trichrome staining (Fig. 3E), or red-colored CFs from picrosirius red staining (Fig. 3F), were observed in the TSS, including in the TL and LCT. Green-colored RFs from picrosirius red staining were also observed in the TL and LCT.

With respect to the direction of fibers, CFs tended to run along the circumference of the silicone tube, and RFs showed randomized running patterns in the TSS. The areas of CFs and RFs appeared to increase with time after surgery.

**Inflammatory features of the TSS during the stable phase**

Fig. 4 shows the inflammatory features examined during the stable phase from D28 to D70. Similar to the reaction phase (Fig. 2A and B), a few $CD3^+$ T cells and $B220^+$ B cells were detected in the LCT, especially around blood vessels, but there were no marked quantitative changes between the examined days (Fig. 4A and B). $Gr\text{-}1^+$ neutrophils were not detected in the TSS of the stable phase (Fig. 4C), but the fusiform $PAD4^+$ reaction was observed inside the TL at only D28, indicating the formation of NETs (Fig. 4D). In toluidine blue staining, metachromatic mast cells were also observed in the LCT in the stable phase, and mast cell numbers tended to increase from D28 to D43 (Fig. 4E). $Iba\text{-}1^+$ macrophages, with spindle or round shapes, were observed mainly in the LCT at D28, and macrophage numbers tended to decrease at D43 and D70 (Fig. 4F).

**Structural components of the TSS in the stable phase**

Angiogenesis and neurogenesis in the TSS were also examined by IHC in the stable phase, from D28 to D70 (Fig. 5A-C). $CD31^+$ vascular endothelial cells and $Tuj\text{-}1^+$ neurons were observed in the resident subcutaneous tissues, and these cells were also seen in the TSS formed after silicone tube embedding, but there were no marked changes between the examined days (Fig. 5A and B), as in the case of the reaction phase. A few $LYVE\text{-}1^+$ lymphatic endothelial cells forming a lumen were detected in the remaining subcutaneous tissues (Fig. 5C). $LYVE\text{-}1^+$ mononuclear cells that did not form vessel structures were scattered in the LCT (Fig. 5C). Compared to D28, the number of $LYVE\text{-}1^+$ mononuclear cells seemed to be higher at D43-70. Furthermore, $\alpha\text{-}SMA^+$ myofibroblasts were detected in the TL on all examined days of the stable phase; they were fusiform in shape and lined the inside of the TL (Fig. 5D). As for the development of fibrous tissues in the TSS, aniline $blue^+$ CFs from Masson's trichrome staining (Fig. 5E), or red-colored CFs from picrosirius red staining (Fig. 5F), were observed in the TSS, including the TL and LCT. Green-colored RFs from picrosirius red staining were also observed in the TL and LCT. With respect to the direction of fibers, CFs tended to run along the circumference of the silicone tube, and RFs showed randomized running patterns in the TSS. The areas of CFs and RFs appeared to increase with time after surgery. Furthermore, these fibers were more developed and denser in the stable phase (Fig. 5E and F) than in the reaction phase (Fig. 3E and F).

**Characteristic inflammatory features in the TSS**

IHC revealed the presence of LYVE-1$^+$ mononuclear cells that did not form LVs in both the reaction and stable phases (Fig. 3 and 5), although the cell type was not clear. As the distributions and shapes of these cells were similar to those of macrophages, double staining for LYVE-1 and Iba-1 was performed at D14, when Iba-1$^+$ macrophages were the most abundant (Fig. 6A). As a result, most LYVE-1$^+$ cells in the TSS were found to be positive for Iba-1.

Fig. 6B and C show the most prominent inflammatory features found at D21 and D28 among the examined samples. Although Gr-1$^+$ neutrophils were scarce from D21 to D70 in most samples (Fig. 2 and 4), numerous Gr-1$^+$ neutrophils remained in the TL and LCT near the silicone tube in these samples (Fig. 6B). Furthermore, strong PAD4$^+$ staining was detected in these samples (Fig. 6C), indicating clearer NETs formation (compared with that observed in Fig. 2D and 4D) and sustained severe inflammation in these mice.

**Indices for histological alterations of the TSS**

Based on our histological observations (Fig. 1-5), we used histoplanimetrical analysis to quantify changes in the histological indices that were altered over time. As shown in Fig. 7A and B, the thickness of the TSS on the skin or visceral side, and that of the TL, showed a tendency to increase in the reaction phase and to decrease in the stable phase; a significant increase in the thickness of the TL was detected at D21 when compared with D2.

As for inflammatory cells, mast cells stained by toluidine blue in the TSS were drastically increased in the reaction phase; mast cell numbers were almost constant during the stable phase, and at D43 were significantly higher than those at D2 (Fig. 7C). The density of Iba-1$^+$ macrophages in the TSS significantly increased at D14 compared with that at D2, and then decreased after that (Fig. 7D). The density of LYVE-1$^+$ cells, which are mononuclear cells (excluding the LV endothelial cells), tended to increase in the TSS with time after surgery (Fig. 7E).

With respect to the collagenous fibers, the area of CF stained by Masson’s trichrome in the TSS increased during the reaction phase, and a significant difference was detected between D2 and D21 (Fig. 7F). Afterward, the area decreased from D21 to D28 and showed constant values in the stable phase. The density of CFs tended to increase during the reaction phase and showed constant values in the stable phase, and the density at D70 was significantly higher than that at D2 (Fig. 7G). Picrosirius red staining revealed that

the relative areas of CFs and RFs tended to increase during the reaction phase; they significantly increased at D28 compared with that at D2 and showed constant values during the stable phase (Fig. 7H). Fig. 7I shows the area ratio of RFs to CFs, and this value was similar during the reaction phase; it decreased at D28 and showed constant values during the stable phase. Significant differences were observed at D28, D43, and D70 compared with that at D2, indicating that CFs and RFs relatively increased and decreased, respectively, in the stable phase.

## Discussion

In the present study, the subcutaneous TSS was comprised of the TL and LCT. Additionally, inflammation and fibrosis were observed in the TSS, and their features were altered with time after surgery. In general, as reported in the previous study [9], the TL is thin but relatively firm, and the LCT, the outer surface of the TL, is slightly rough. Indeed, the TSS in the present study was easily removed from the surface of the visceral tissues during sampling. Thus, the TSS has been referred to as the "fibrous capsule" since the 1930s [9]. Furthermore, the shape of the TSS was almost homogenous among the silicone tubes, and there was no difference in thickness between the skin and visceral sides of the TSS. In general, silicone is considered to be a low-reactive material, and silicone breast implants have been widely used for more than 50 years in plastic surgery [23]. Thus, the homogeneity of materials and shapes of the foreign body may strongly affect the histological features of the formed TSS.

In this study, the main feature of the foreign body reaction in the reaction phase was the innate immune response, characterized by infiltration of macrophages and neutrophils. In particular, the net number of macrophages was significantly higher than that of neutrophils. Macrophages are known to mediate foreign body reactions through their phagocytic function of degrading foreign bodies [24]. In addition to these direct actions on the foreign body, macrophages can also produce biological factors, such as transforming growth factor beta (TGF-β) and platelet-derived growth factor [12],[14], to promote fibrosis. In particular, TGF-β is crucial for the transformation of fibroblasts into myofibroblasts, and this process is important for actuating the formation of fibrotic tissue by generating a capsule around the foreign body [12]. Indeed, we found that the number of macrophages in the TSS significantly increased at D14, and this timing corresponded with the appearance of α-SMA$^+$ myofibroblasts in the TL. Activated fibroblasts or myofibroblasts can produce an extracellular matrix containing collagen [12]. Importantly, the thickness of the TL and the area of the LCT containing CFs significantly increased at D21, suggesting that the fibrotic function of myofibroblasts was present in the TSS. Thus, macrophages in the TSS are important for degradation of the foreign body, and for covering it with fibrotic tissues via the activation of myofibroblasts through humoral factors.

As for macrophages, we newly identified LYVE-1$^+$ macrophages in the TSS, and their counts tended to increase with time after surgery. A previous study indicated that LYVE-1$^+$ macrophages are involved in angiogenesis. Briefly, the recruitment, infiltration, and accumulation of bone marrow-derived LYVE-1$^+$ macrophages are crucial for the

formation of a dense vascular network in adipose tissue [25]. Macrophages play important roles in lymphangiogenesis, particularly in macrophage subpopulations that express LYVE-1 [26]. Importantly, a previous study showed that accelerated wound healing was associated with a reduced number of M1 macrophages and induction of nitric oxide production, whilst the number of prohealing CD206- and LYVE-1-expressing M2 macrophages was maintained [27]. Strikingly, we found an increase in LYVE-$1^+$ macrophages with the progression of time following surgery and considered that LYVE-$1^+$ macrophages would be associated with stable fibrosis. Further phenotypic clarification of M1 and M2 macrophages would be interesting in future research into foreign body reactions. Clear angiogenesis or lymphangiogenesis was not observed in the TSS in the present study. In contrast, LYVE-$1^+$ macrophages surrounding the aorta degrade collagen by recruiting hyaluronan on smooth muscle cells, thereby preventing arterial stiffness by controlling the expression of collagen in smooth muscle cells [28]. Furthermore, in the present study, mast cell numbers also increased with time after surgery, although the net number was lower than that of macrophages. A previous study indicated that angiogenesis was stimulated by histamine, which is locally secreted by mast cells [12]. In contrast, another study indicated that mast cell tryptase promoted fibroblast proliferation [29]. Thus, LYVE-$1^+$ macrophages or mast cells may play a crucial role during the foreign body reaction; however, clear angiogenesis or lymphangiogenesis was not demonstrated in the present study. Therefore, these cells may have a role in regulating foreign body reactions through collagen remodeling or increasing fibroblasts, rather than through angiogenesis/lymphangiogenesis.

At the early stage of foreign body reactions, neutrophils also migrate and accumulate around the silicone tube. Although activated neutrophils are generally considered to function as phagocytes to defend the host, a recent study discovered that neutrophils release histone-containing extracellular nucleic acids, called NETs [13]. NETs are able to trap and kill various extracellular pathogens by providing a highly concentrated supply of antimicrobial compounds, and the process of NET formation with neutrophil death is called NETosis [30]. Interestingly, high levels of PAD4, a marker of NETosis, were detected during D2-28, and clear localization of $PAD4^+$ cells was detected at the TL from D7, although Gr-$1^+$ neutrophils were detected during D2-14. Furthermore, net-like structures of $PAD4^+$ reactions were clearer in mice showing more severe inflammation in the TSS. Therefore, neutrophils reduced the cellularity, as indicated by the reduced expression of Gr-1 at D21-28, but they may try to protect the host tissues by covering the foreign body through formation of NETs. As there are few reports about NETosis in

foreign body reactions, our results provide a novel finding regarding the role of neutrophils in this process.

Compared with the reaction phase, there were no marked histological changes in the stable phase, but histoplanimetrical analyses revealed a clear change in the synthesis of connective tissue. The area of connective tissues showed the highest values at D21, and the area ratio of CFs and RFs increased until D28, indicating the initiation of connective tissue synthesis after infiltration of macrophages, as observed at D14. During the increase in CFs, the levels of other extracellular matrix components, such as glycosaminoglycans and proteoglycans, also increase [(12)], and these extracellular matrix components are related to the interactions between CFs. Indeed, the density of CF was higher during D21-70, suggesting that the attachment of CFs became strict. Therefore, it is possible that the number of CFs may increase and CFs may be contracted at the stable phase in the foreign body reaction. In addition, the appearance ratio of CF and RF differed during the observation period. CFs were abundant in the stable phase, whereas RFs were abundant in the reaction phase. As RFs are mainly found in lymphoid tissues [(31)], these results indicate the difference in histological status in the TSS, such as inflammatory conditions resembling those in pathologically-induced lymphoid tissues or fibrotic conditions.

The various stages of the foreign body reaction found in the TSS are summarized in Figure 8. After subcutaneous embedding of the silicone tube, inflammatory cells, CFs, and RFs accumulated around the silicone tube at D2. The TSS is composed of two layers, the TL and LCT. From D7, the formation of NETs by neutrophils was observed in the TL. At D14, the number of macrophages significantly increased compared to that at D2, and then myofibroblasts emerged in the TL owing to the action of factors secreted by macrophages. At D21, the thickness of the TL and the area of the LCT, containing CFs, significantly increased by myofibroblast action. Based on the histological characteristics, we refer to D2-21 as the reaction phase. At D28, the appearance ratio of CF and RF changed in the TSS. At D70, the density of the connective tissue significantly increased. We refer to D28-70 as the stable phase. Furthermore, mast cells and LYVE-1$^{+}$ macrophages remained in the TSS to maintain the fibrotic process during the stable phase.

In conclusion, our study demonstrated that the TSS is composed of the TL and LCT, and that the foreign body reaction involves two phases. In the reaction phase, neutrophils and macrophages mainly function in innate immunity. In the stable phase, development and stabilization of the connective tissue takes place, and the tissues mature within almost one month. In contrast, maintenance of severe inflammation would affect the transition

to the stable phase, as observed in severe NETosis. The present study provides insights into the pathogenesis of foreign body reactions and their application in advanced medical technologies such as iBTA.

**Acknowledgement**

NA

**Funding**

This work was supported in part by a Japan Society for the Promotion of Science (JSPS) KAKENHI grant (grant no. 17H02101).

**Author contributions**

S.O., O.I., T.N., and Y.K. designed the experiments. S.O., M.A.M., and T.N. performed the experiments. S.O. and O.I. analyzed the data. Y.O. and T.N. supervised the experimental techniques. M.A.M., T.N., and Y.N. reviewed the manuscript. All authors were involved in writing the paper and have approved the final manuscript.

## References


1. Kurtz SM, Devine JN. PEEK biomaterials in trauma, orthopedic, and spinal implants. Biomaterials 2007;28:4845-4869.
2. Ward WK, Slobodzian EP, Tiekotter KL, Wood MD. The effect of microgeometry, implant thickness and polyurethane chemistry on the foreign body response to subcutaneous implants. Biomaterials 2002;23:4185-4192.
3. Ward WK, Wood MD, Troupe JE. Rise in background current over time in a subcutaneous glucose sensor in the rabbit: Relevance to calibration and accuracy. Biosens Bioelectron 2000;15:53-61.
4. Vascellari M, Mutinelli F, Cossettini R, Altinier E. Liposarcoma at the site of an implanted microchip in a dog. Vet J 2004;168:188-190.
5. Vepari C, Kaplan DL. Silk as a biomaterial. Prog Polym Sci 2007;32:991-1007.
6. Griffith LG. Polymeric biomaterials. Acta Mater 2000;48:263-277.
7. Banaszkiewicz PA. Reactions of the articular capsule to wear products of artificial joint prostheses. Class Pap Orthop 2014;11:77-79.
8. Matsuno H, Yokoyama A, Watari F, Uo M, Kawasaki T. Biocompatibility and osteogenesis of refractory metal implants, titanium, hafnium, niobium, tantalum and rhenium. Biomaterials 2001;22:1253-1262.
9. Nakayama Y, Ishibashi-Ueda H, Takamizawa K. In vivo tissue-engineered small-caliber arterial graft prosthesis consisting of autologous tissue (biotube). Cell Transplant 2004;13:439-449.
10. Low SP, Voelcker NH, Canham LT, Williams KA. The biocompatibility of porous silicon in tissues of the eye. Biomaterials 2009;30:2873-2880.
11. Livet V, Pillard P, Goy-Thollot I, Maleca D, Cabon Q, Remy D, Fau D, Viguier É, Pouzot C, Carozzo C, Cachon T. Placement of subcutaneous ureteral bypasses without fluoroscopic guidance in cats with ureteral obstruction: 19 cases (2014–2016). J Feline Med Surg 2017;19:1030-1039.
12. Luttikhuizen DT, Harmsen MC, Luyn MJ. Cellular and molecular dynamics in the foreign body reaction. Tissue Eng 2006;12:1955-1970.
13. Yipp BG, Kubes P. NETosis: How vital is it? Blood 2013;122:2784-2794.
14. Desai NP, Hubbell JA. Tissue response to intraperitoneal implants of polyethylene oxide-modified polyethylene terephthalate. Biomaterials 1992;13:505-510.
15. Prem R, Acharya BLG, Mathews J, Ambadas, Jagtap P, Bhavsar B. Indications for dental implant

518 treatment- a clinician’s point of view. IJCRR 2014;6:29-33.

519 16. Terazawa T, Nishimura T, Mitani T, Ichii O, Ikeda T, Kosenda K, Tatsumi E, Nakayama Y. Wall
520 thickness control in biotubes prepared using type-C mold. J Artif Organs 2018;21:387-391.

521 17. Nakayama Y, Kaneko Y, Okumura N, Terazawa T. Initial 3-year results of first human use of an
522 in-body tissue-engineered autologous "Biotube" vascular graft for hemodialysis. J Vasc Access
523 2020;21:110-115.

524 18. Nakayama Y, Furukoshi M, Terazawa T, Iwai R. Development of long in vivo tissue-engineered
525 "Biotube" vascular grafts. Biomaterials 2018;185:232-239.

526 19. Ishii D, Enmi JI, Iwai R, Kurisu K, Tatsumi E, Nakayama Y. One year rat study of iBTA-induced
527 "Microbiotube" microvascular grafts with an ultra-small diameter of 0.6 mm. Eur J Vasc
528 Endovasc Surg 2018;55:882-887.

529 20. McBeath R, Pirone DM, Nelson CM, Bhadriraju K, Chen CS. Cell shape, cytoskeletal tension,
530 and RhoA regulate stem cell lineage commitment. Dev Cell 2004;6:483-495.

531 21. Schneider CA, Rasband WS, Eliceiri KW. NIH Image to ImageJ: 25 years of image analysis. Nat
532 Methods 2012;9:671-675.

533 22. Hinz B, Phan SH, Thannickal VJ, Galli A, Bochaton-Piallat ML, Gabbiani G. The myofibroblast:
534 one function, multiple origins. Am J Pathol 2007;170:1807-1816.

535 23. Dolores W, Christian R, Harald N, Hildegunde P, Georg W. Cellular and molecular composition
536 of fibrous capsules formed around silicone breast implants with special focus on local immune
537 reactions. J Autoimmun 2004;23:81-91.

538 24. Sussman EM, Halpin MC, Muster J, Moon RT, Ratner BD. Porous implants modulate healing
539 and induce shifts in local macrophage polarization in the foreign body reaction. Ann Biomed Eng
540 2014;42:1508-1516.

541 25. Cho CH, Koh YJ, Han J, Sung HK, Lee HJ, Morisada T, Schwendener RA, Brekken RA, Kang
542 G, Oike Y, Choi TS, Suda T, Yoo OJ, Koh GY. Angiogenic role of LYVE-1-positive
543 macrophages in adipose tissue. Circ Res 2007;100:e47-e57.

544 26. Kubota Y, Takubo K, Shimizu T, Ohno H, Kishi K, Shibuya M, Saya H, Suda T. M-CSF
545 inhibition selectively targets pathological angiogenesis and lymphangiogenesis. J Exp Med
546 2009;206:1089-1102.

547 27. James L, Rodero MP, Patel J, Moi D, Mazzieri R, Khosrotehrani. Interleukin-23 regulates
548 interleukin-17 expression in wounds, and its inhibition accelerates diabetic wound healing
549 through the alteration of macrophage polarization. FASEB J 2018, 32:2086-2094.

550 28. Lim HY, Lim SY, Tan CK, Thiam CH, Goh CC, Carbajo D, Chew SHS, See P, Chakarov S,

Wang XN, Lim LH, Johnson LA, Lum J, Fong CY, Bongso A, Biswas A, Goh C, Evrard M, Yeo KP, Basu R, Wang JK, Tan Y, Jain R, Tikoo S, Choong C, Weninger W, Poidinger M, Stanley RE, Collin M, Tan NS, Ng LG, Jackson DG, Ginhoux F, Angeli V. Hyaluronan receptor LYVE-1-expressing macrophages maintain arterial tone through hyaluronan-mediated regulation of smooth muscle cell collagen. Immunity 2018;49:326-341.e7.

29. Ruoss SJ, Hartmann T, Caughey GH. Mast cell tryptase is a mitogen for cultured fibroblasts. J Clin Invest 1991;88:493-499.

30. Steinberg BE, Grinstein S. Unconventional roles of the NADPH oxidase: signaling, ion homeostasis, and cell death. Sci STKE 2007;2007:1-5.

31. Midori, H., Muta, K. and Takeshi H. Direct contact between reticular fibers and migratory cells in the paracortex of mouse lymph nodes: a morphological and quantitative study. Arch Histol 1988;51:233-240.

## Figure legends

**Figure 1. Histological characteristics of the subcutaneous TSS**

Histology of the TSS with skin under low magnification (A). The TSS was observed beneath the skin (asterisks), and the silicone tube was missing due to the process of sectioning or staining. The TSS developed with time after surgery and appeared to expand perpendicular to the viscera–skin axis (arrows) from D28. Hematoxylin and eosin staining. Bars = 1 mm.

Histology of the TSS with skin under high magnification (B). The TSS was composed of the TL (arrows), and LCT containing mononuclear cells, and their development differed among days after surgery. Some of the D21 samples showed well-developed TSS with severe cell infiltration. CM: Cutaneous muscle, D: Day, LCT: Loose connective tissues, N: Nerve, TL: Thin layer, TSS: Tissue surrounding silicone tube. Hematoxylin and eosin staining. Bars = 100 μm.

**Figure 2. Inflammatory features of the TSS in the reaction phase**

Immunohistochemistry (IHC) for CD3 (A) and B220 (B), markers for T cells and B cells, respectively, revealed the presence of a few T and B cells around the LCT. IHC for Gr-1 (C), a neutrophil marker, revealed that the neutrophils were mainly localized in the TL or LCT on D2-14 post-surgery, but not at D21. Staining for PAD4, a marker of neutrophil extracellular traps (NETs) formation, was detected mainly in the TL at D7-21 (D). Metachromatic mast cells identified by toluidine blue staining were also detected in the LCT with increases seen over time (E). IHC for Iba-1, a marker for macrophages, revealed the presence of numerous macrophages in the LCT (F). D: Day, LCT: Loose connective tissue, TL: Thin layer. Arrowheads indicate positive cells. Bars = 100 μm.

**Figure 3. Structural components of the TSS in the reaction phase**

Immunohistochemistry (IHC) for CD31 (A) and Tuj-1 (B), markers for vascular endothelial cells and neurons, respectively, revealed the presence of these cells in the LCT or resident tissues, without remarkable changes over time. IHC for LYVE-1, a marker for lymph vessels, revealed that LYVE-1-positive lymph vessels with lumen were scarce, but LYVE-1$^+$ mononuclear cells were scattered in the LCT. α-SMA$^+$ cells lining the TL, indicating myofibroblasts, appeared from day 14 post-surgery (D14) (D). Bars = 100 μm.

Connective tissues were evaluated by Masson's trichrome (E) and picrosirius red (F) staining. Masson's trichrome staining revealed that aniline blue$^+$ connective tissues in the LCT increased with time. The TL also showed dense staining for aniline blue (insets). Bars = 500 μm. Picrosirius red staining revealed the presence of red- and green-colored collagen and reticular fibers; both fibers tended to increase in the LCT and TL (insets) with time. CM: Cutaneous muscle, D: Day, LCT: Loose connective tissue; TL: Thin layer. Asterisks identify skin and arrowheads indicate positive cells. Bars = 100 μm.

**Figure 4. Inflammatory features of the TSS in the reaction phase**

Immunohistochemistry (IHC) for CD3 (A) and B220 (B), markers for T cells and B cells, respectively, revealed a few positive cells in the LCT. IHC for Gr-1 (C), a neutrophil marker, revealed an absence of neutrophils on D28-70 post-surgery. Cells positive for PAD4, a marker of neutrophil extracellular trap formation, were detected mainly in the TL at D28 (D). Metachromatic mast cells from toluidine blue staining were also detected in the LCT with time-related increases (E). IHC for Iba-1, a marker for macrophages, revealed numerous macrophages in the LCT (F). D: Day, LCT: Loose connective tissue, TL: Thin layer. Asterisks identify cutaneous muscle, and arrowheads indicate positive cells. Bars = 100 μm.

**Figure 5. Structural components of the TSS in the reaction phase**

Immunohistochemistry (IHC) for CD31 (A) and Tuj-1 (B), markers for vascular endothelial cells and neurons, respectively, revealed positive cells in the LCT or resident tissues without marked changes over time. IHC for LYVE-1, a marker for lymph vessels, revealed that LYVE-1-positive lymph vessels with lumen were scarce, but LYVE-1$^+$ mononuclear cells were scattered in the LCT (C). α-SMA$^+$ cells lined the TL, indicating myofibroblasts (D). Bars = 100 μm.

Connective tissues were evaluated by Masson's trichrome (E) and picrosirius red (F) staining. Masson's trichrome staining revealed that aniline blue$^+$ connective tissues in the LCT increased with time. The TL also showed dense aniline blue$^+$ reactions (insets). Bars = 500 μm. Picrosirius red staining revealed the presence of red- and green-colored collagen and reticular fibers; both fibers tended to increase in the LCT and TL (insets) with time. D: Day, LCT: Loose connective tissue, TL: Thin layer, CM: Cutaneous muscle. Asterisks identify skin, and arrowheads indicate positive cells. Bars = 100 μm.

**Figure 6. Histological characteristics of samples showing severe inflammation**

A. Co-expression of LYVE-1 (green) and Iba-1 (red) in the LCT of samples on D14 after surgery, when macrophages were the most abundant. Several double-positive cells were observed in the TSS. Bars = 100 μm.

B and C show the immunohistochemistry images for Gr-1 and PAD4 (markers for neutrophils and neutrophil extra trap formation, respectively) in the samples showing severe inflammation (D21 and D28). In addition to abundant Gr-1$^+$ cells in the TL and LCT, reticular and numerous PAD4$^+$ reactions were observed near the TL. LCT: Loose connective tissue, TL: Thin layer, ST: Silicone tube, D: Day. Arrowheads indicate positive cells. Bars = 100 μm.

**Figure 7. Indices for histological alterations of the TSS**

TSS thickness of the skin and visceral sides (A). TL thickness (B). Number of mast cells in the TSS (C). Macrophage density (D). Density of LYVE-1$^+$ cells (E). CF area (F). CF density (G). Area ratios of CF and RF (H). Area ratio of RF/CF (I). Each bar represents mean ± SE (n = 4). *: Significance compared to D2 (Kruskal–Wallis test followed by Dunnett's test, $P < 0.05$. CF: Collagen fiber, D: Day, RF: Reticular fiber, TSS: Tissue surrounding silicone tube.

**Figure 8. Schematic diagram representing histological alterations in the TSS**

Neu: Neutrophils, MC: Mast cells, Mac: Macrophages, LYVE-1$^+$ mac: LYVE-1$^+$ macrophages, Myo: Myofibroblasts, CF: Collagen fibers, RF: Reticular fibers, BV: Blood vessels, NETs: Neutrophil extracellular traps, ST: Silicone tubes, TL: Thin layer, D: day.

**Table 1. List of antibodies used in this study**

| Antibody | Host | Dilution | Source | Antigen retrieval | Blocking serum |
|---|---|---|---|---|---|
| Gr-1 | Rat | 1 :800 | R and D system, Minnesota, USA | Pepsin | 10% normal goat serum |
| Iba-1 | Rabbit | 1 :1200 | Wako, Tokyo, Japan | Tris | 10% normal goat serum |
| CD3 | Rabbit | 1 :200 | Nichirei, Tokyo, Japan | Tris | 10% normal goat serum |
| B220 | Rat | 1 :1600 | Cedarlane, Burlington, Canada | Pepsin | 10% normal goat serum |
| Tuj-1 | Mouse | 1 :10000 | Abcam, Cambridge, UK | CB | 10% normal goat serum |
| CD31 | Rabbit | 1 :100 | Abcam, Cambridge, UK | Tris | 10% normal goat serum |
| LYVE-1 | Rabbit | 1 :500 | Adipogen, San Diego, USA | CB | 10% normal goat serum |
| PAD4 | Rabbit | 1 :100 | Abcam, Cambridge, UK | Tris | 10% normal goat serum |
| α-SMA | Rabbit | 1 :3000 | Abcam, Cambridge, UK | CB | 10% normal goat serum |
| Iba-1 | Mouse | 1:1000 | Wako, Tokyo, Japan | CB | 5% Donkey normal serum |
| Rat IgG-biotin | Goat | 1 :400 | BioLegend, San Diego, CA, USA | | |
| Rabbit IgG-biotin | Goat | Undiluted | Undiluted SABPO®Kit, Nichirei, Tokyo, Japan | | |
| Mouse IgG-biotin | Goat | 1 :100 | Catalog Medysystems, Buckingham, UK | | |
| Rabbit IgG-Alexa Fluor 488 | Donkey | 1 :500 | Thermo Fisher Scientific, Waltham, MA, USA | | |
| Mouse IgG-Alexa Fluor 546 | Donkey | 1 :500 | Thermo Fisher Scientific, Waltham, MA, USA | | |
| Pepsin: 0.1% pepsin, 37°C, 5min | | | | | |
| Tris: 20mM tris(hydroxymethyl)aminomethane-HCl (pH9.0), 110°C, 15min | | | | | |
| CB: 10nM citrate buffer (pH6.0), 110°C, 15min | | | | | |

Figure 1

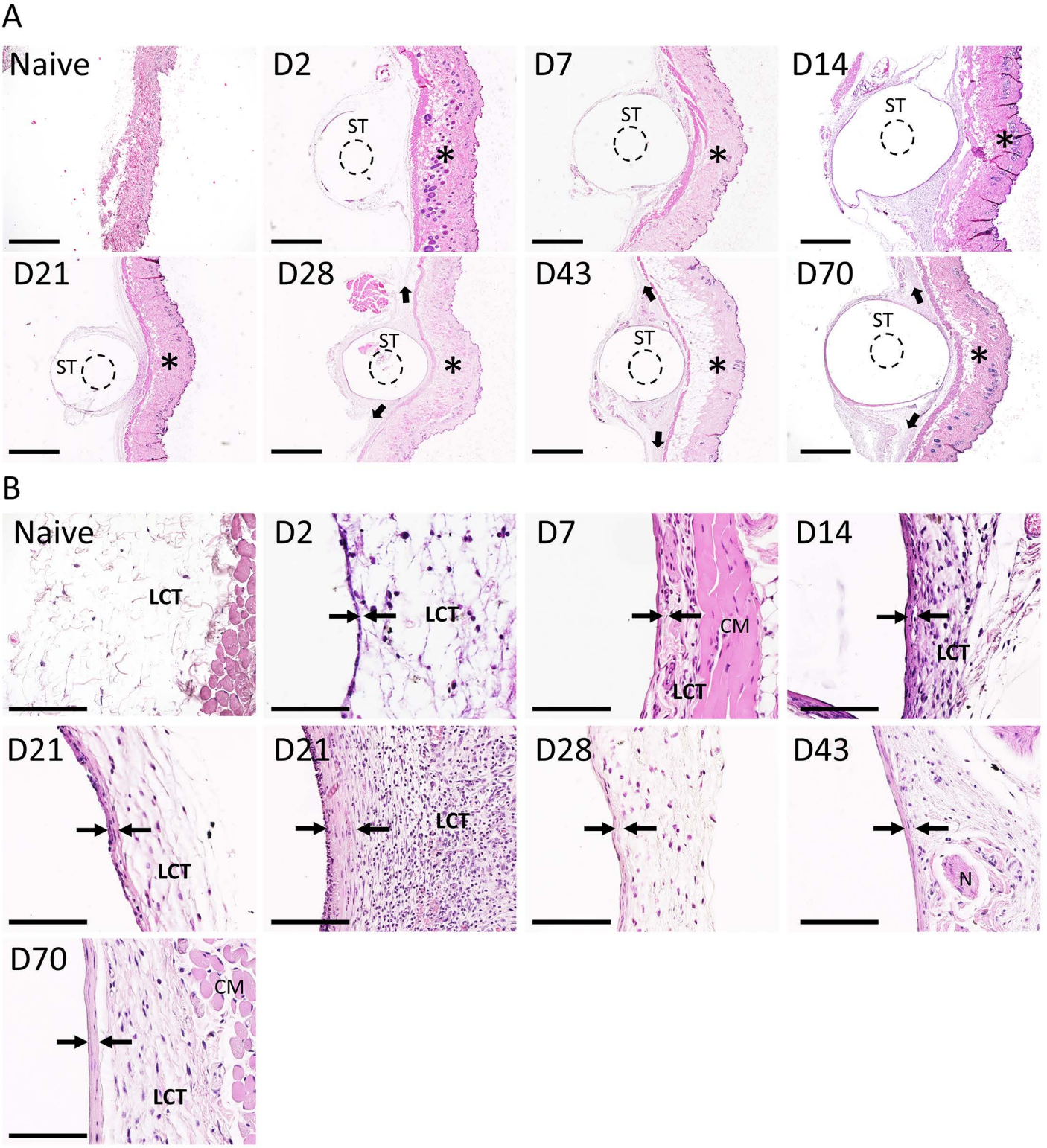
A
Naive
D2
D7
D14
D21
D28
D43
D70
ST
B
Naive
D2
D7
D14
D21
D21
D28
D43
D70
LCT
CM
N

Figure 2

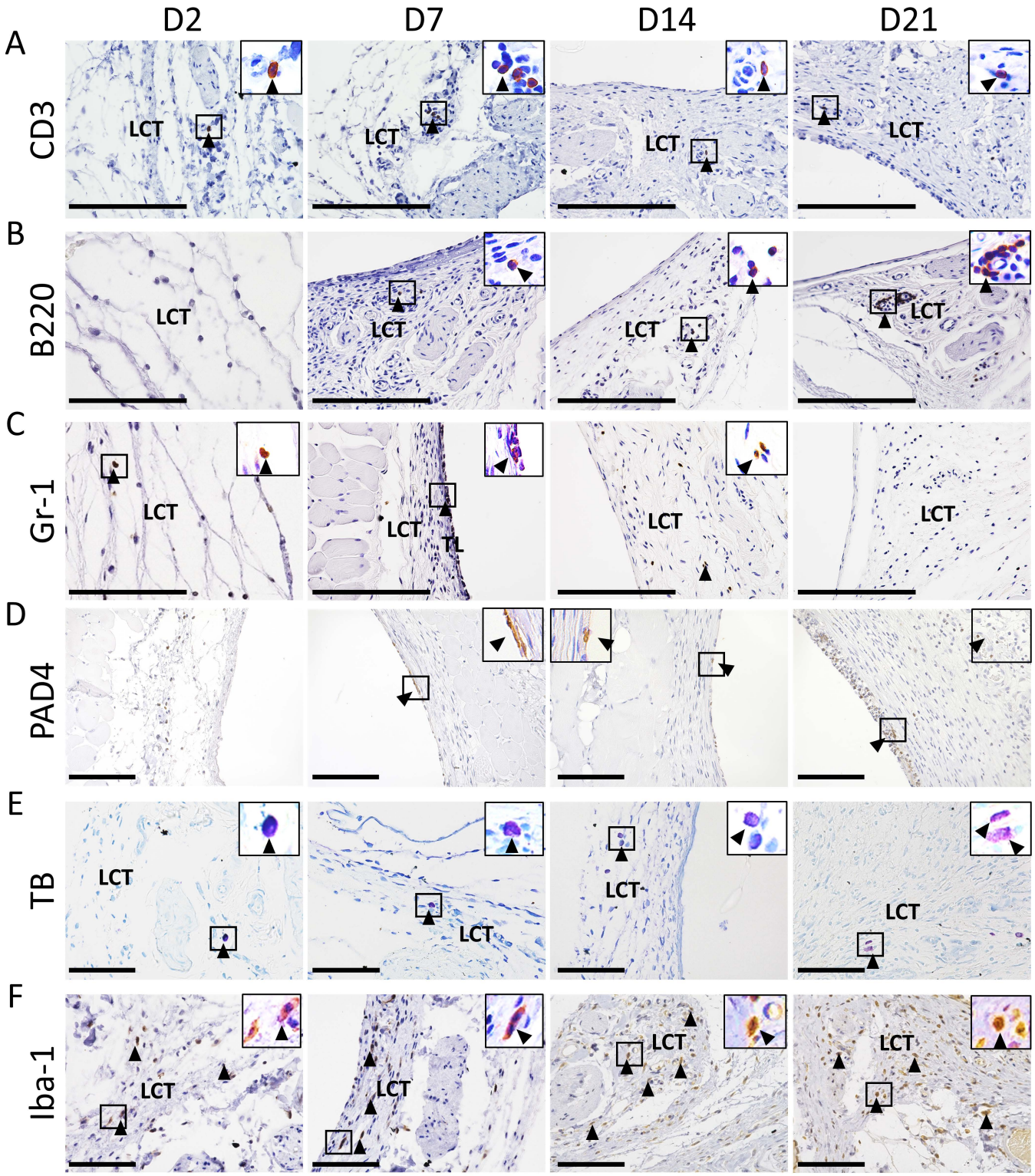

Figure 5

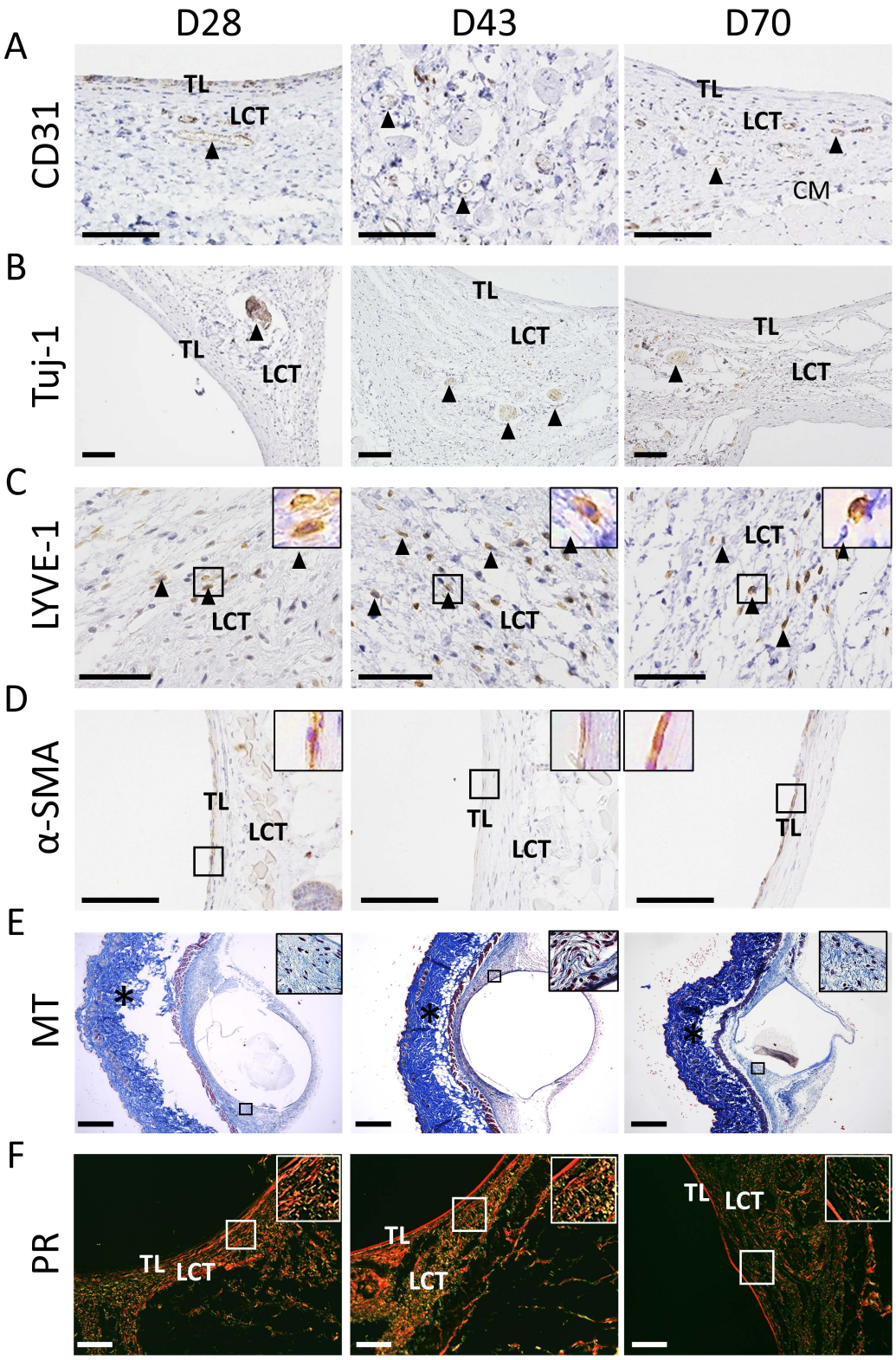

Figure 4

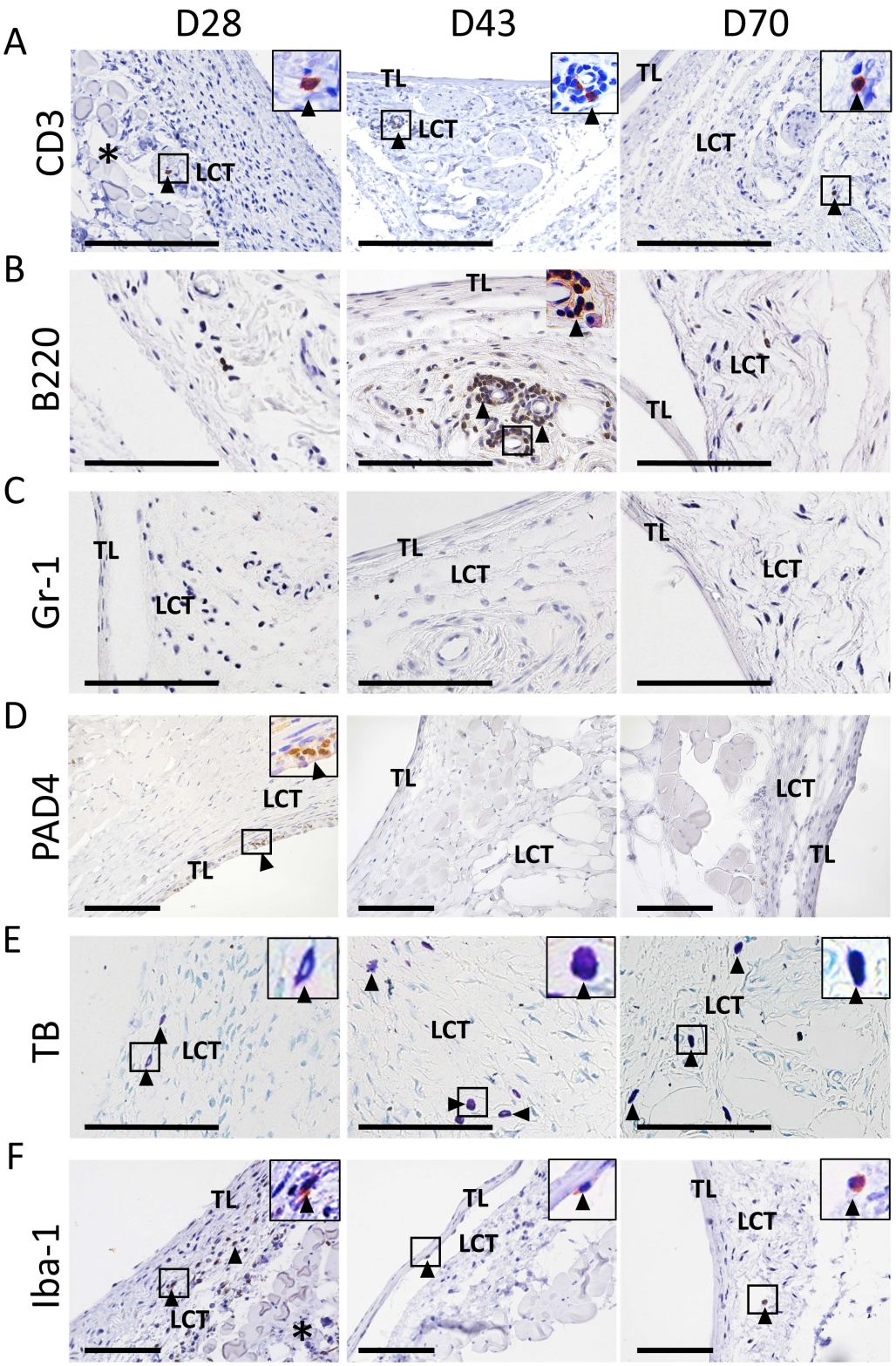

Figure 5

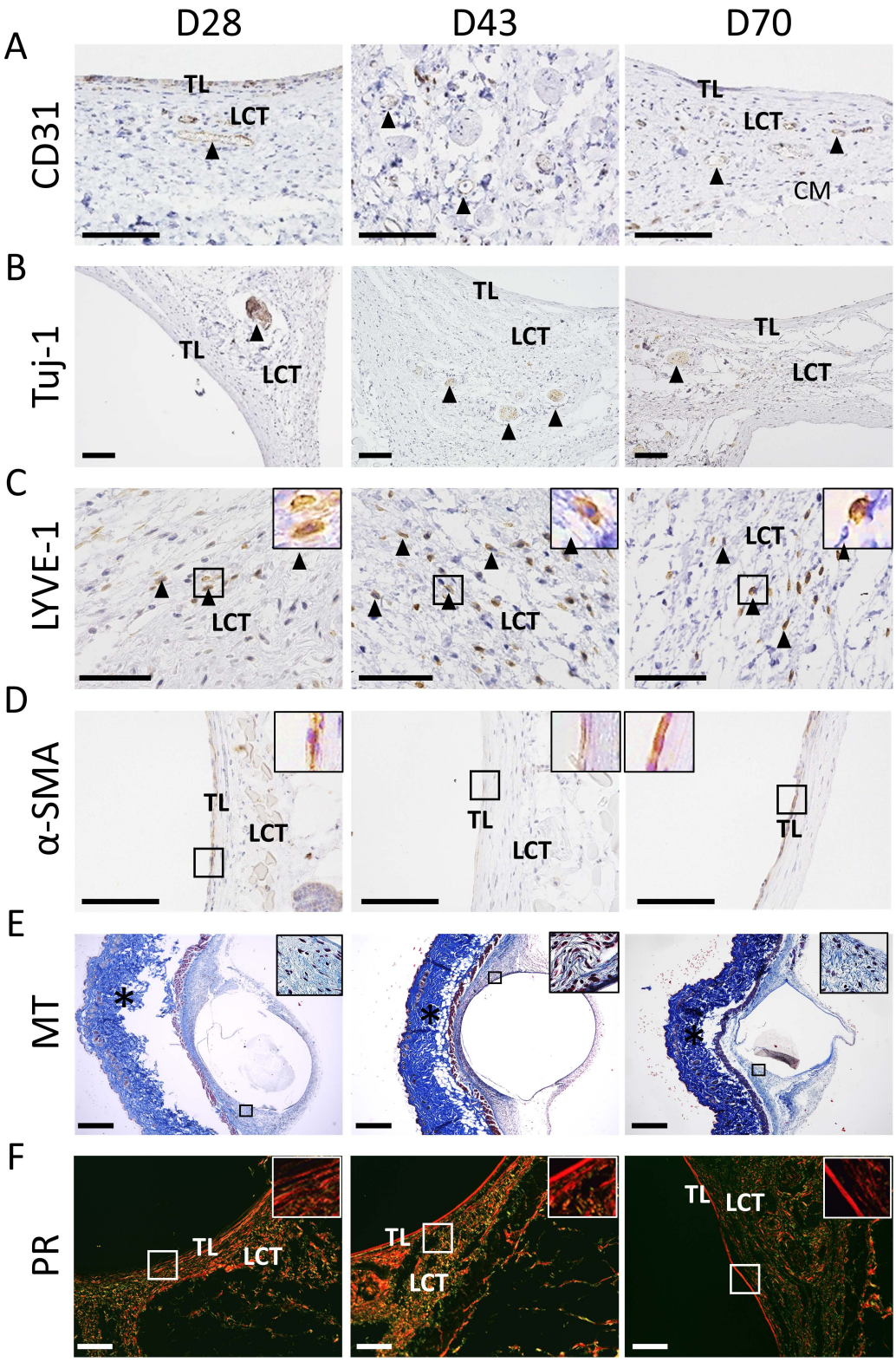

Figure 6

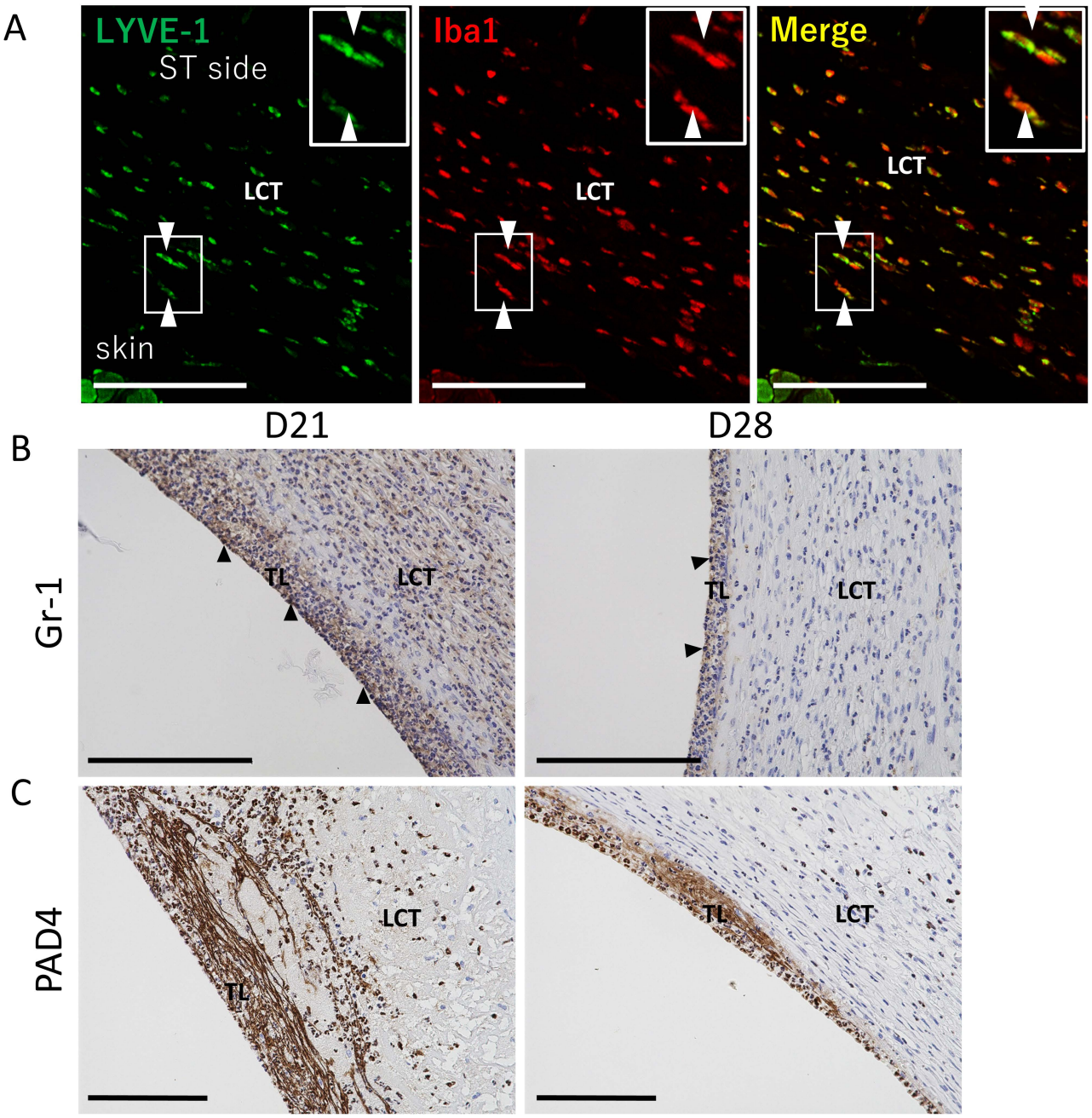
A
LYVE-1
ST side
LCT
skin
Iba1
LCT
Merge
LCT
D21
D28
B
Gr-1
TL
LCT
TL
LCT
C
PAD4
LCT
TL
TL
LCT

Figure 7

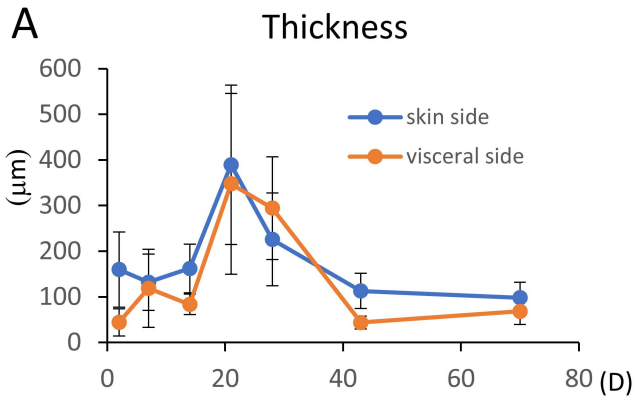
A
Thickness
skin side
visceral side
(μm)
(D)

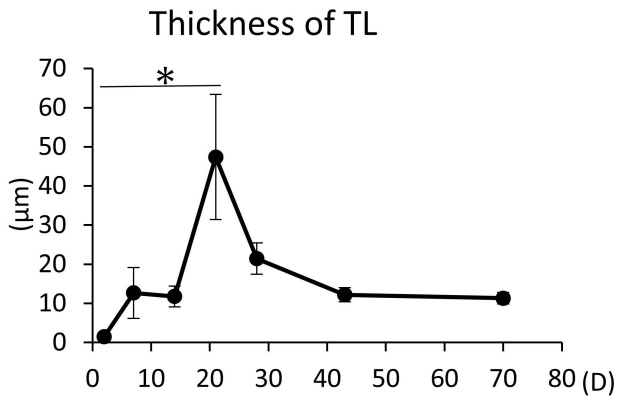
B
Thickness of TL
*
(μm)
(D)

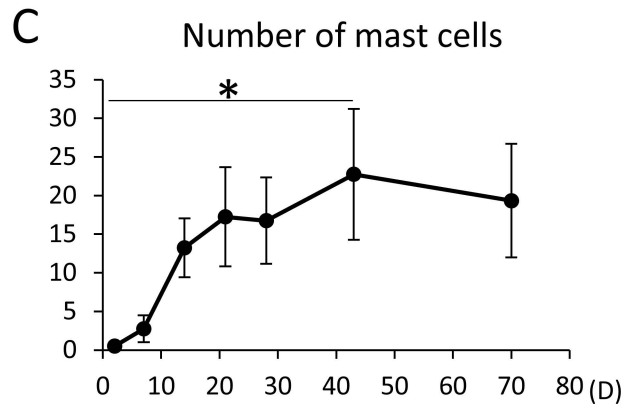
C
Number of mast cells
*
(D)

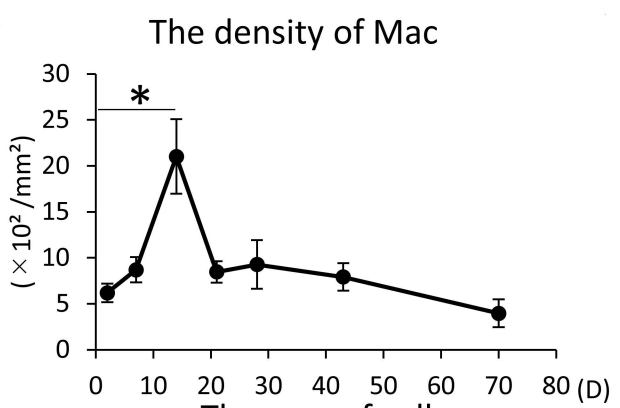
D
The density of Mac
*
(×10² /mm²)
(D)

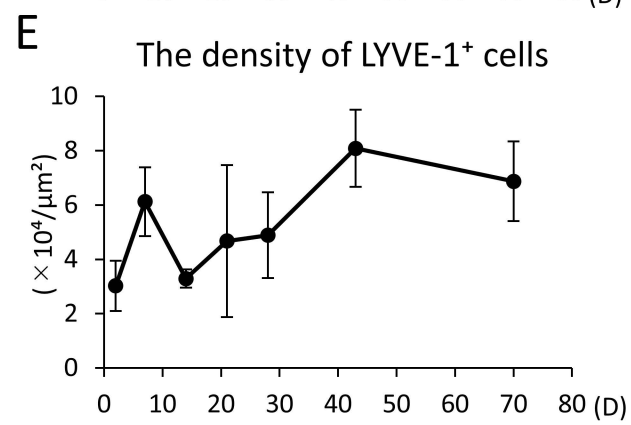
E
The density of LYVE-1⁺ cells
(×10⁴/μm²)
(D)

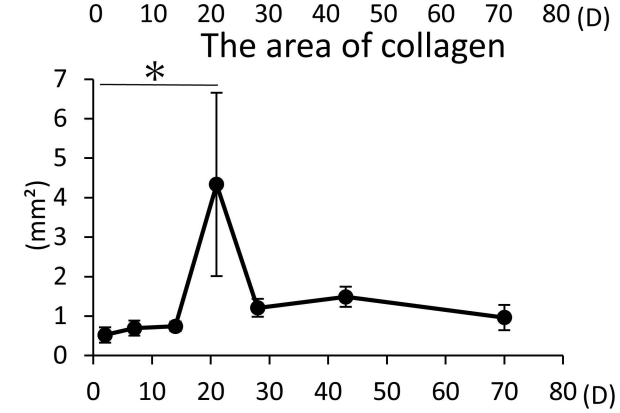
F
The area of collagen
*
(mm²)
(D)

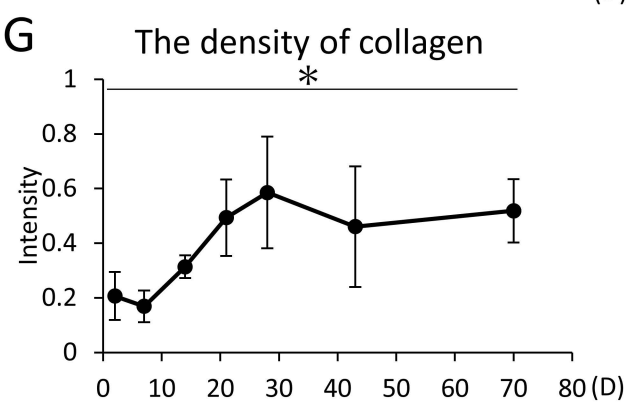
G
The density of collagen
*
Intensity
(D)

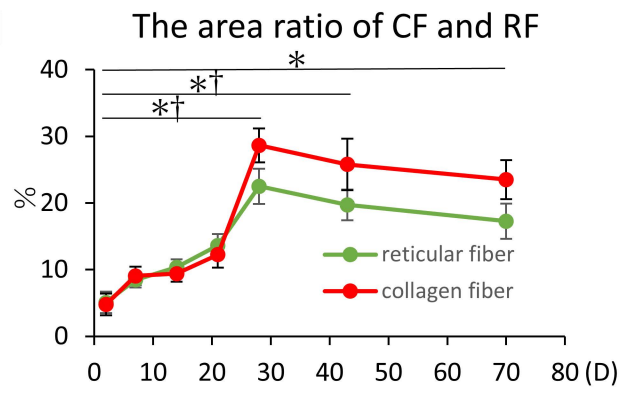
H
The area ratio of CF and RF
*
*†
*†
%
reticular fiber
collagen fiber
(D)

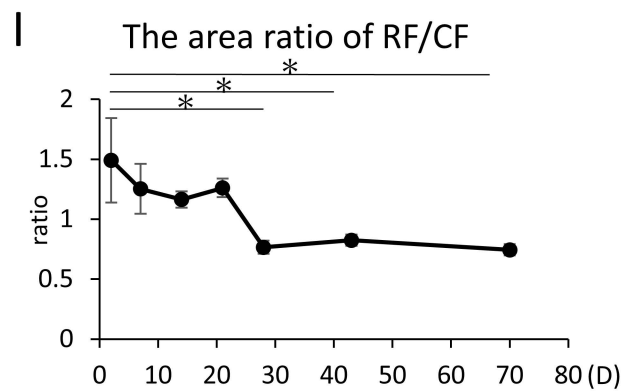
I
The area ratio of RF/CF
*
*
*
ratio
(D)

Figure 8

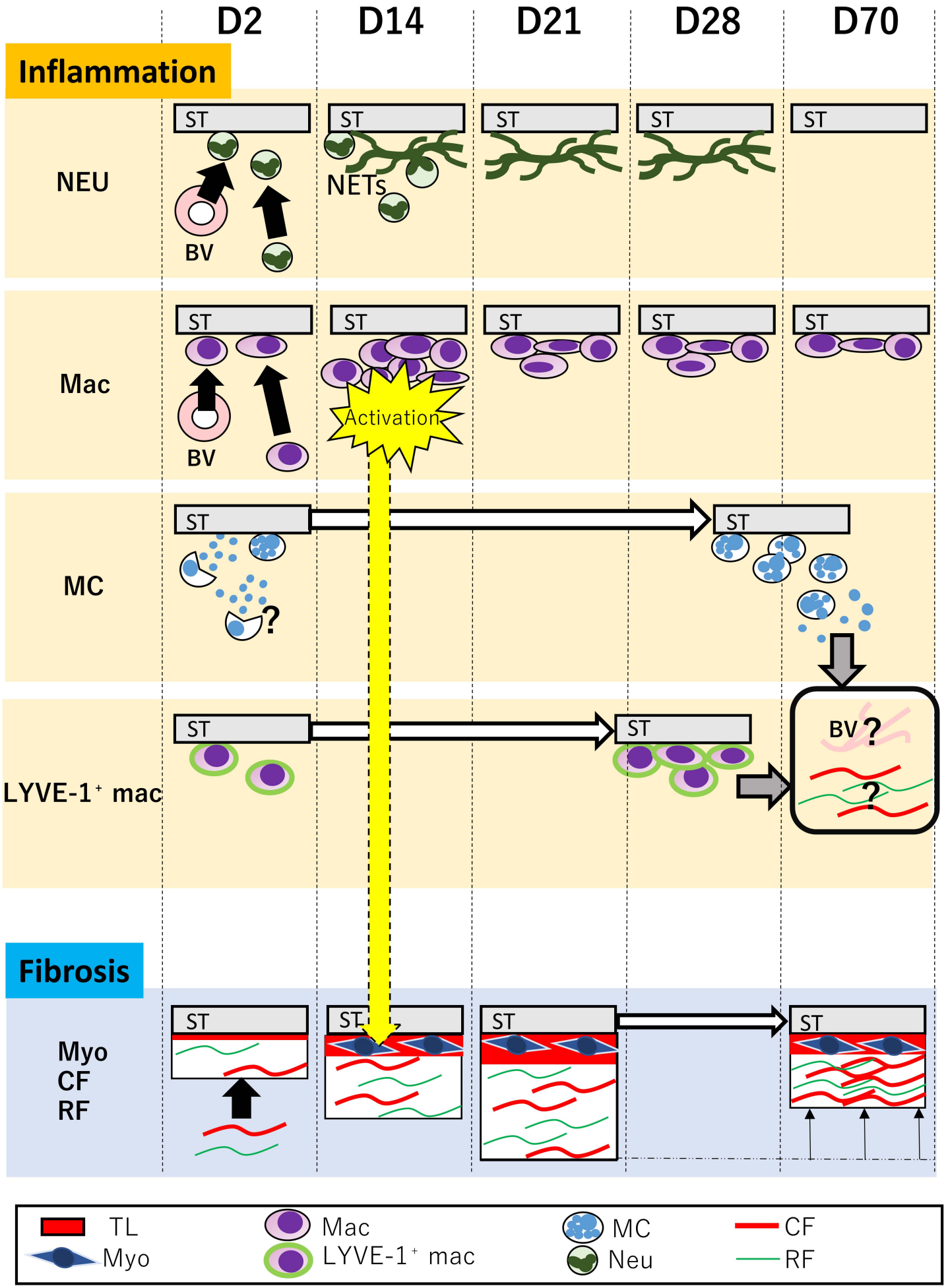
D2
D14
D21
D28
D70
Inflammation
NEU
ST
NETs
BV
Mac
Activation
MC
?
LYVE-1⁺ mac
BV ?
Fibrosis
Myo
CF
RF
TL
Myo
Mac
LYVE-1⁺ mac
MC
Neu
CF
RF